Quantitative autoradiography in boron neutron capture therapy considering the particle ranges in the samples

Satoshi Takeno[a,b], Hiroki Tanaka[a], Tsubasa Watanabe[a], Takashi Mizowaki[b] and Minoru Suzuki[a,*]

[a] Particle Radiation Oncology Research Center, Institute for Integrated Radiation and Nuclear Science, Kyoto University, Osaka, Japan

[b] Department of Radiation Oncology and Image-Applied Therapy, Kyoto University, Kyoto, Japan

* Corresponding author (E-mail address: suzuki.minoru.3x@kyoto-u.ac.jp)

Abstract

Boron neutron capture therapy is a cellular-scale particle therapy exploiting boron neutron capture reactions in boron compounds distributed in tumour cells. Its therapeutic effect depends on both the accumulation of boron in tumour cells and the neutron fluence. Autoradiography is used to visualise the micro-distribution of boron compounds. Here, we present an equation for the relationship between boron concentration and pit density on the solid-state nuclear track detector, taking into consideration the particle ranges in the samples. This equation is validated using liver-tissue sections and boron standard solutions; it reproduces the experimentally observed trends between boron concentration and pit density. The equation in this paper provides a theoretical explanation for the widely used calibration curve between pit density and boron concentration; it also provides a method to correct for differences of tissue-section thickness in quantitative autoradiography. Moreover, we present a simple co-localisation system for pit and tissue-section images that requires no special equipment. Using the equation together with this co-localisation system could improve micro-scale quantitative estimation in tissue sections.

Keywords

Boron neutron capture therapy, Autoradiography, Microdistribution

1. Introduction

Boron neutron capture therapy (BNCT) is a next-generation particle therapy. A tumour is irradiated after the administration of a borated formulation able to concentrate in tumour cells. The boron neutron capture reaction (BNCR) occurring inside the tumour cells releases charged particles able to destroy the cells. If the boron uptake is restricted only to tumour cells, these can be irradiated without damaging the surrounding normal cells, as the ranges of the alpha particles and recoiled lithium nuclei emitted from the BNCR are shorter than 9 µm, that is, less than the size of single cells [1]. Therefore, BNCT can be used as a cellular-scale particle therapy. The therapeutic effect depends on the boron accumulation in tumour cells and on the neutron fluence. It is thus essential to clarify the boron distribution in the tissue at the cellular level in order to maximise the effectiveness of BNCT.

The most common methods for measuring the boron concentration are Inductively Coupled Plasma - Atomic Emission Spectrometry (ICP-AES), Prompt Gamma-ray Analysis (PGA), Secondary-Ion Mass Spectrometry (SIMS), Alpha Spectrometry, and Autoradiography (ARG) [2,3]. Of these, only SIMS and ARG can show the boron distribution in the tissue at the cellular level visually. SIMS has high resolution but requires special equipment [4], whereas ARG provides enough resolution for analysis without any requiring special equipment except a neutron source [5]. Consequently, ARG is widely used for analysing boron distribution in tissues. In ARG, tissue samples are placed on a solid-state nuclear track detector (SSNTD) and irradiated with a thermal-neutron beam. The micro-scale distribution of the alpha particles and recoiled lithium nuclei emitted from the BNCR is revealed by pits detected on the SSNTD [6,7].

One way to quantify boron concentration is to estimate the pit density from the thermal-neutron fluence and boron concentration theoretically. The equation for the pit density has been reported as follows [8]:

$$\rho_{pit} = C(B) \cdot \frac{N_v \sigma_B \varphi}{4} \cdot (R_\alpha cos^2\theta_\alpha + R_{Li}cos^2\theta_{Li}), \tag{1}$$

where ρ_{pit} is the pit density; $C(B)$ the concentration of boron; N_v the number of atoms per unit volume; σ_B the neutron cross-section of ^{10}B; φ the thermal-neutron fluence; R_α and R_{Li} the ranges of alpha particles and recoiled lithium nuclei, respectively; and θ_α and θ_{Li} the critical angles of the alpha particles and recoiled lithium nuclei, respectively. However, this equation is known to reproduce the experimental results poorly [9].

Using Monte Carlo simulation to understand the track formation process in BNCR has been attempted in the past [9]. The gap that exists between the simulated and measured pit densities in such an approach has been explained as the observation efficiency.

The density of the pits measured by ARG is thought to correlate with the concentration of boron compounds. A widely used method that takes advantage of this to quantify the boron concentration is the

calibration curve method, in which the pit density of a sample is compared to that of a reference material [6,10,11]. However, the material density and elemental compositions of the tissue sections and reference material are not equivalent, and furthermore, it is necessary to consider the effects of water loss because the material density and elemental composition of tissue sections on the SSNTD vary with this process [12]. One needs to be careful in comparing the measured pit density of a sample with that of the reference material because the ranges of alpha particles and recoiled lithium nuclei vary depending on the material density of the tissue sections. One answer to this problem is to introduce the evaporation coefficient (CEv):

$$CEv = m_{dry}/m_{ori},$$

(2)

where m_{ori} is the mass of the original sample before evaporation and m_{dry} is the mass of dried sample after evaporation. CEv can be used to convert weight reduction to thickness change [12,13].

In this paper, we present a new equation to estimate the pit density from the boron concentration and thermal-neutron fluence by considering the differences in the material densities and elemental compositions of the samples, that is, the particle-range differences within them. Using this equation, we propose a new model of the relationship between BNCR and pit formation on the SSNTD. Then, we validate this new model using liver tissue sections and a boron standard solution. We also describe a co-localisation system to analyse the spatial distribution of boron compounds in the tissue sections.

2. Materials and methods

2.1 Development of equation to estimate pit density

We propose the following equation to estimate the pit count (N [counts]) from the tissue-section thickness (t [μm]), boron concentration (C [μg/g]), material density of the original tissue section (d [g/cm^3]), neutron fluence (ϕ [n/cm^2]), and area of the region of interest (S [μm^2]):

$$N = \left(\int_0^t P_{alpha}(x)\, dx + \int_0^t P_{Li}(x)\, dx \right) \cdot \frac{N_A \cdot \sigma}{MW} \cdot 10^{-18} \cdot \phi \cdot C \cdot d \cdot S,$$

(3)

where $P_{alpha}(x)$ and $P_{Li}(x)$ are the expected detection probabilities of the alpha particles and recoiled lithium nuclei, respectively; MW is the molecular weight of boron [g/mol]; N_A is the Avogadro constant [/mol]; and σ is the neutron cross-section of ^{10}B [cm^2]. We have attached the Microsoft Excel file for calculating pit density using this equation as supplementary data.

In the estimation of $P_{alpha}(x)$ and $P_{Li}(x)$ in equation (3), we have introduced the concept of a 'region of undetectability' in which we cannot recognise pits on the SSNTD by using an optical microscope. The thickness of the region of undetectability is termed the 'undetectability thickness'. Further details are given in the Appendix.

4

2.2 Determination of the parameters in the equation: charged particle ranges and critical angles

2.2.1 Determination of the ranges of the alpha particles and recoiled lithium nuclei.

The mean ranges of alpha particles and recoiled lithium nuclei in various dried tissue sections, water, and the CR-39 (BARYOTRAK) SSNTD were determined using the Monte Carlo particle-transport simulation code PHITS 3.20 [14]. Here, we define 'mean range' as the range at which the linear energy transfer of the particles is reduced to half of its maximum value.

To obtain the ranges with PHITS, one needs the material density and elemental composition of the material in which the particles are propagating. For dried tissue sections, these must be determined by experiment. We prepared five BALB/c mice (CLEA Japan, Tokyo, Japan), and inoculated them subcutaneously with CT26 cells (kindly given by Dr Hironobu Yanagie) in their thighs (5×10^5 cells per mouse) to make a tumour xenograft model. Then, we resected livers, kidneys, muscles, spleens, and tumours (CT26). Each organ was put in a test tube to dry naturally at room temperature and room humidity. We measured its weight manually twice a week and judged it to have dried when the weight decreases stabilised to a plateau. In this measurement, we considered the weight of the whole organ, not of a thin tissue section, to reduce the uncertainty related to the weight change due to support materials such as Optimal Cutting Temperature Compound.

We assumed that the elemental composition of the original tissue samples was that described in ICRU REPORT 46 (human normal tissue elemental composition). With this assumption, the dried-tissue elemental composition is estimable by eliminating the H_2O component from the original elemental composition. The weight of the H_2O component to be eliminated was assumed to be equivalent to the weight change in the drying process. Assuming the volume does not change in the evaporation process, the material density of dried tissue (d_{dry}) is

$$d_{dry} = d_{ori} \cdot CEv, \qquad (4)$$

where d_{ori} is the material density of original tissue and CEv is the evaporation coefficient mentioned in equation (2). (The validity of the constant-volume assumption is discussed in section 4.1.2.) The material density of the original tissue was extrapolated from the value in ICRU REPORT 46. For the water components of organs other than those measured in this experiment, we used literature data [15].

In the calculation using PHITS, the material density of CR-39 was set to 1.32 g/cm^3 and its elemental composition was set to $C_{12}H_{18}O_7$, following the literature [16].

Both in this process and later ones, the mice were handled according to the Recommendations for the Handling of Laboratory Animals for Biomedical Research, compiled by the Committee on Ethical Handling

Regulations for Laboratory Animal Experiments, Kyoto University. All animal experiments were performed in accordance with institutional laboratory-animal-handling guidelines.

2.2.2 Relationship between material density and charged particle ranges in dried tissue sections.

To estimate the ranges of charged particles by the method of the previous section, the material density and elemental composition of the tissue sections must be known. However, the elemental composition is sometimes unclear. For example, when ARG is performed on tumour-tissue sections, the elemental composition is largely unknown because of the section's heterogeneity. On the other hand, the material density of dried tissue can be acquired easily by comparing the weights before and after the drying process.

In this work, we calculated the relationship between the material density and the mean ranges of the charged particles using model tissue sections. We chose average soft tissue from adult males (ICRU REPORT 46) as a model tissue. Although the density of the model tissue is 1.03 g/cm^3, we assumed for the calculation that the value was somewhere between 0.10 and 1.00 g/cm^3. The ranges of alpha particles and recoiled lithium nuclei were estimated under this condition using PHITS 3.20. Fitted curves were calculated using the least-squares method.

Then, to validate the fitted curves, we compared them with mean ranges in various dried organs calculated in the previous section.

2.2.3 Critical angles of alpha particles and recoiled lithium nuclei.

Although the critical angles of alpha particles and recoiled lithium nuclei were unclear under these experimental conditions, we assumed that they were small enough to be masked by the effect of the region of undetectability, the thickness of which we estimated under this assumption. Then, we analysed the distribution of pit depths on the CR-39 and measured the undetectability thickness to validate our estimate (the details are explained in section 2.6). If the measured undetectability thickness is consistent with the estimated undetectability thickness, we infer that our assumption was reasonable.

2.3 ARG of tissue sections

2.3.1 Preparing tissue sections.

^{10}B-enriched L-p-boronophenylalanine (L-BPA) was purchased from Interpharma, Prague, Czech Republic. It was mixed with fructose in distilled water. Then, NaOH was added to increase the pH to above

10 so that the L-BPA would dissolve more easily. After this, 1N HCl was added to adjust the pH to 7.6. The L-BPA solution was adjusted to be 3 wt% solution.

This L-BPA solution was administered subcutaneously into nuchal sites in nine-week-old female BALB/c mice (CLEA Japan, Tokyo, Japan). All the mice were normal and without any treatment. We varied the L-BPA dosage from 500 mg/kg to 2000 mg/kg in order to change the boron concentration accumulated in the liver. The mice were then sacrificed, and their livers were resected. The details of the administered L-BPA-solution dosages and the times from administration to sacrifice are listed in Table 1. The timing of sacrifice was typically 1h after administration, a period in which the BPA concentration in the liver remains high according to our previous study [17]. However, in order to observe low accumulation in the liver, mice nos. 5 and 6 were sacrificed 3h and 17h after administration, respectively. In mouse no. 9, L-BPA was administered in two instalments in order to prevent the leakage of subcutaneous injections. The liver was divided into two parts: one for ARG and the other for ICP-AES.

After resection, the liver samples for ARG were frozen rapidly using hexane chilled by liquid nitrogen as a refrigerant. Then, they were sliced into thicknesses of 4–12 μm and pasted onto CR-39 using a cryostat. After pasting on CR-39, the tissue sections were dried at room temperature and room humidity.

The liver samples for ICP-AES were digested with perchloric acid (60%) and hydrogen peroxide solution (30%) for 12 h at 75 °C, referring to our previous study [17]. Then, their boron concentration was analysed using ICP-AES (Shimadzu ICPE-9000) in order to calibrate the undetectability thickness and validate the estimated boron concentration by ARG in section 2.5.

2.3.2 Neutron irradiation, chemical etching, and observation.

The tissue sections on CR-39 were irradiated with a thermal-neutron beam at Kyoto University Research Reactor (KUR) [18]. During the irradiation, the thermal-neutron fluence was measured using gold activation foils (Fig. 1). The irradiation time, which was chosen to keep the pit density measurable, ranged from 7 to 15 minutes at a thermal power of 1 MW. Short irradiation times correspond to low rates of BNCR, and therefore to high boron concentrations in the samples. In this experiment, the thermal-neutron fluence was from 6.32×10^{11} n/cm^2 to 1.36×10^{12} n/cm^2.

After irradiation, we acquired the tissue-section images. To facilitate the superposition of the histological image and the pit image, we used a ball-point pen to put small ink-mark close to the place to be analysed but on the opposite side of CR-39 from the tissue section. (Although the places to be analysed were chosen randomly in this experiment, it may be possible to choose them by referring to an already-stained continuous section.) Then, the CR-39 was placed on the slide glass using epoxy resin adhesive to avoid the disappearance of the ink-mark during the chemical etching process (Fig. 2). We performed Hematoxylin–

Eosin (HE) staining using Canada balsam, which can be easily removed by xylene, as a sealant. Then we acquired tissue images and corresponding ink-mark images (Fig. 3(A) (B)) using an optical microscope (Keyence BZ-9000).

After observation of the HE-stained image, we removed the sealant and the tissue section on CR-39 using xylene. Subsequently, we performed a chemical etching process using PEW solution (15 wt% KOH + 65 wt% EtOH + 20 wt% H_2O). The etching time was eight minutes with a temperature of 50 °C, following the protocol in the literature [11]. We used the PEW solution to minimise pits from sources other than BNCR and selected a relatively low-temperature protocol to avoid deformation of the ink-marks.

After the etching process, we acquired the pit images. We identified the location of the liver section on CR-39 using the ink-marks. Then, we acquired a ink-mark image and a pit image corresponding to the HE-stained images (Fig. 3(C) (D)). We could then superimpose the HE and pit images precisely using the ink-marks (Fig. 4). Thus, we could check the tissue sections corresponding to the pit images. We obtained 12 images for each sample (some images were without corresponding HE images).

2.3.3 Analysis of the pit images.

The pit density was obtained from the pit images using a custom-made computer program written in Python 3.7.7, with the OpenCV 4.2.0 library. The program enabled us to perform the analysis as follows:

Each image of the pits was binarised and the contours of the pits were detected. To avoid under-estimating the pit density, pits that overlapped were identified and separated by their shape and the distribution of pixel values (Fig. 5). The automatically detected pits were validated visually. The analysis omitted areas in which pit detection was affected by noise, such as unwanted marks on the detector.

From the 12 pit images, we adopted 10 pit-density results, excluding the highest and lowest densities. We defined the average of these 10 densities as the pit density of the sample.

2.4 ARG of the boron standard solution

The boron standard solution (H_3BO_3) was purchased from Wako (Osaka, Japan). Its ^{10}B concentration was adjusted to 4.975, 9.950, 19.90, or 39.80 μg/g by diluting the original solution, assuming a ^{10}B percentage of 19.9%. This range was determined as the boron concentration in clinical conditions (administration of L-BPA 500mg/kg body weight) [17]. Two samples of boron standard solution were prepared for each concentration. Then, we packed 3 mL of each solution and a CR-39 in a low-density polyethylene bag (Fig. 6).

8

The plastic bags containing the boron standard solution and CR-39 samples were irradiated with a thermal-neutron beam at KUR (Fig. 6). The irradiation time was 3 minutes at a thermal power of 5 MW. Their fluence was measured using gold activation foils one by one; it ranged from 5.98×10^{11} n/cm^2 to 8.12×10^{11} n/cm^2.

The process for etching the CR-39 samples was the same as for the ARG of the tissue sections (shown in section 2.3.2). Then, each CR-39 was observed under an optical microscope using four fields of view per concentration (a total of eight observations, since there were two samples of boron standard solution at each concentration), and its pit density was analysed using the pit-detection program of section 2.3.3.

2.5 Comparison of estimated and measured pit densities

The undetectability thickness must be determined before the comparison between estimated and measured pit densities can be made. We measured the pit density at various boron concentrations in 10 or 12 µm-thick tissue sections in section 2.3. In this analysis, the thickness of the tissue sections was standardised to 12 µm and the thermal-neutron fluence was standardised to 8.0×10^{11} n/cm^2 using equation (3). We also estimated the pit densities by the same equation, using boron concentrations measured by ICP-AES as parameters in the equation. Next, we compared the measured pit densities with the estimated ones to determine the most suitable undetectability-thickness value, i.e. the one with the smallest coefficient of determination (R^2). This calculation was performed using Python 3.7.7, with the SciPy 1.4.1 library.

After determining the undetectability thickness, we compared the measured pit densities for tissue sections of various thicknesses (4–12 µm) in section 2.3 to the estimated pit densities using the determined parameters. We also compared the measured pit densities corresponding to various concentrations of the boron standard solution (4.975–39.80 µg/g) in section 2.4 to the estimated pit densities using the determined parameters. In these comparisons, the thermal-neutron fluence was standardised to 8.0×10^{11} n/cm^2.

2.6 Examination of the undetectability thickness

When we observe the pits under an optical microscope, the image changes depending on the plane of focus, as shown in Fig. 7. For plane (2) in Fig. 7, the pit disappears and its colour changes from black to white. Here, we assume that this plane is related to the deepest point of the pit. Then, we can measure the relative pit depth by analysing the Z-Stack image of the pits. Z-Stack pit images (captured at 0.1 µm intervals) were obtained using an optical microscope (Keyence BZ-9000) and analysed via a custom-made computer program written in Python 3.7.7 with the OpenCV 4.2.0 library.

The undetectability thickness can be calculated using (Fig. 8):

9

$$u = r - (l_{deepest} - l_{shallowest}),\tag{5}$$

where u is the undetectability thickness, r is the particle range, $l_{deepest}$ is the deepest pit depth, and $l_{shallowest}$ is the shallowest pit depth.

By calculating the difference between the depths of the deepest and shallowest pits, we can calculate the undetectability thickness. For this analysis, we used the two CR-39s with the smallest tilt, as keeping the CR-39 horizontal is essential when analysing the relative pit depth. The difference in depth between the two ends of the region of interest (ROI) becomes smaller if the ROI is separated into smaller areas. For this reason, since it is technically difficult to make the CR-39 completely horizontal, each was divided into 12 small areas to minimise the gap of the focused plane between both ends of the area.

Owing to the effect of straggling of charged particle ranges, the undetectability thickness measured here is expected to vary. We assumed that the distribution follows a normal distribution and estimated the interval of undetectability thickness. Then, we estimated the 95% confidence interval of the mean of the population for the undetectability thickness. The statistical analysis was performed using Python 3.7.7, with the SciPy 1.4.1 library.

3. Results

3.1 Determination of the parameters in equation (3)

3.1.1 Determination of the mean ranges of the charged particles.

The CEv and estimated mean ranges for each organ are listed in Table 2(A). According to the data, the water content of adipose tissue is extremely low, which may cause variations in the ratio of the water component in the liver owing to the state of the liver, for example, depending on whether the liver is healthy or fatty. The ranges of the charged particles in the dried organs listed here were also estimated using PHITS (Table 2(A)).

The relationship between the material density and the range of the charged particles under the elemental composition of average soft tissue was estimated and fitted curves were calculated. According to the fitted curves, the mean ranges of the alpha particles (r_{alpha} [µm]) and recoiled lithium nuclei (r_{Li} [µm]) were, respectively,

$$r_{alpha} = 7.53 \cdot d^{-1.00}$$
$$r_{Li} = 3.81 \cdot d^{-1.00},\tag{6}$$

where d is the material density [g/cm^3]. If we know the original material density before water loss (d_{ori} [g/cm^3]) and the CEv, then r_{alpha} and r_{Li} become

10

$$r_{alpha} = 7.53 \cdot (d_{ori} \cdot CEv)^{-1.00}$$
$$r_{Li} = 3.81 \cdot (d_{ori} \cdot CEv)^{-1.00},$$

(7)

using equation (4). Particle ranges estimated using PHITS (Table 2(A)) were compared with ranges calculated by equation (7) (Fig. 9). The coefficients of determination (R^2) of r_{alpha} and r_{Li} from equation (7) and from PHITS estimation were 0.993 and 0.986, respectively.

From the above results, the mean ranges of alpha particles and recoiled lithium nuclei in dried tissue sections can be calculated from their original material density and CEv via equation (7). If the material density of the original tissue is unknown, that of average soft tissue (1.03 g/cm^3) can be used as an approximation. This provides a simple method for estimating the mean ranges of charged particles without using Monte Carlo simulation—very useful, especially in the case of tissues of unknown elemental composition, such as tumour sections.

We also estimated the mean ranges of charged particles in CR-39 and water using PHITS, as listed in Table 2(B).

3.1.2 Determination of the undetectability thickness.

We calibrated the undetectability thickness by comparing the estimated and measured pit densities at various boron concentrations. In this pit-density estimation, we used the boron concentration in liver-tissue sections measured using ICP-AES (Table 1) as a parameter of equation (3). We determined an undetectability thickness of 2.37 µm (Fig. 10). The coefficient of determination (R^2) between the estimated and measured pit densities was 0.975.

3.2 Comparison of the estimated and measured pit densities

3.2.1 Measured pit density for various concentrations of the boron standard solution.

We compared the measured and estimated pit densities for a boron standard solution using the undetectability thickness estimated in the previous section. The results are shown in Fig. 10.

There is a difference between the estimated and measured pit densities, which can be attributed to the possible difference in the undetectability thickness between the standard boron solution and the tissue sections. In the process of ARG of tissue sections, the staining process includes the use of many reagents, such as xylene and ethanol, that may attack the surface of the CR-39 and alter the undetectability thickness. If the boron concentration is invariant, then the pit density in the boron standard solution is almost one-third of the pit density in the dried liver sections. Although there is a gap between the measured and

estimated pit densities, this estimation method reproduces the trend of the actual data for the liver-tissue sections and boron standard solution.

3.2.2 Measured pit densities of tissue sections with various thicknesses.

We compared the measured and estimated pit densities for various tissue-section thicknesses ranging from 4–12 µm. The relationship of tissue-section thickness to the estimated and measured pit densities is shown in Fig. 11.

Although the estimated pit density follows the same trend as the measured, there is a gap between them, especially for thinner layers. According to the estimated curve, the influence of errors associated with the tissue-section thickness becomes more pronounced in thinner sections. Potential factors responsible for errors in thinner sections include the cutting accuracy of the cryostat and technical errors when affixing tissue sections to CR-39. Because the errors in Fig. 11 seem to be systematic errors, the low accuracy of the cryostat is considered the most likely source for the discrepancy.

3.3 Examination of the undetectability thickness

The distribution of the undetectability thickness is shown in Fig. 12. The interval of the population mean of the undetectability thickness is 2.30 < undetectability thickness < 2.71 (95% confidence interval).

Previously, we estimated the undetectability thickness to be 2.37 µm, which is consistent with the result here. In this study, we assumed that the critical angles were sufficiently small to be masked by the effect of the region of undetectability; our results show that this assumption can be considered reasonable.

4. Discussion

4.1 Relationship between new equation and already reported quantitative ARG

4.1.1 Introduction of the concept of region of undetectability.

We introduced the concept of a region of undetectability in equation (3). In previous attempts to understand the pit formation process in the BNCR, the gap between estimated and measured pit density has been explained as observation efficiency [9]. Thus, the concept of region of undetectability in this paper may correspond to the concept of observation efficiency.

The undetectability thickness is an important variable that needs to be determined experimentally. Its value varies with the experimental conditions. The storage condition of the SSNTD [16], the attack by reagents during the staining process (suggested in section 3.2.1), the chemical-etching method [19], the pit-

observation method, and the pit-detection software are considered to be the foremost factors that affect the undetectability thickness. Theoretically, once the undetectability thickness has been determined, it can be used to inform further estimates as long as the experiments are made under identical conditions. However, if any of the conditions are changed, the undetectability thickness must be redetermined for the new conditions. Moreover, since the undetectability thickness can be affected by many factors, we recommend calibrating this value in each experiment if possible.

4.1.2 Reflection of the evaporation effect in sections.

In the widely used calibration-curve method, there are several ways to reflect the effect of evaporation on sections. One of these is to introduce a CEv to convert the weight change of the sample to a thickness change, as described in section 1 [12,13]. For example, if the weight of the sample is halved, then the thickness of the sample is assumed also to be halved, while the density remains the same as the original density. Another method is to use a homogenised mixture of liver cells and a solution of BPA in different fixed proportions [20,21]. The reliability of these approaches has already been cross-validated [22,23]. The method to keep the tissue sections on SSNTD frozen during the ARG process is known [24,25], and it is also effective for considering the effects of drying.

In this paper, we assume that the thickness of the sample does not change in the evaporation process, but that the material density changes instead. According to equation (6), the material density and the mean range of the charged particle have an inverse relationship. Moreover, in terms of the remaining ranges through the sample, the change of particle ranges can be converted into the change of thickness using their inverse relationship when we consider the impact of energy loss of the particles in the sample. Hence, the difference of material density under the assumption of fixed thickness can be converted into the difference of thickness under the assumption of fixed density. In reality, we consider both density and thickness change due to water loss. To avoid underestimating the position error of the pit due to the charged particle entering diagonally in future analysis, we choose to assume it is the thickness that is constant [7].

We need data on the elemental composition and material density for PHITS calculation to estimate the ranges of the charged particles. We can estimate them in dried condition from the original elemental composition, original density, and CEv, as shown in section 2.2.1. However, in the case of certain tissues such as tumour, the elemental composition and material density are unknown. In that case, we can estimate ranges only from the CEv using equation (7), extrapolating from the data of average soft tissue described in section 3.1.1.

4.1.3 The effect of thickness on pit density

13

According to Fig. 11, if the tissue sections are thin, a small experimental error associated with the thickness becomes amplified to a significant error in the pit density. The uncertainty of the pit density in thinner sections is also mentioned in the literature [13]. Therefore, for precise boron-concentration measurements, using thick tissue sections is preferable. By contrast, tissue staining is more effective for thin tissue sections. Another advantage of thin tissue sections is that they reduce the error associated with the pit positions and the locations where BNCRs occur [7]. Considering this, the thickness of the tissue sections should be determined based on the purpose of the experiment.

4.1.4 Comparison of new and previous approaches to quantitative ARG

As already explained, the calibration curve method is widely used for quantitative ARG. The method in this paper is the attempt to express the calibration curve as an equation. Calibrating the undetectability thickness (section 2.5), we can obtain the calibration curve as equation (3). Once we have determined the undetectability thickness, we can estimate the calibration curves of other sample materials or tissue sections with different thicknesses by inserting the parameters (such as particle ranges and original density) in equation (3) without experimentally drawing the calibration curve again, as long as the experimental conditions are unchanged. Particle ranges can be estimated using PHITS, given the material composition, original density, and CEv. Even if we do not have the data on the material composition and original density, equation (7) enables us to extrapolate the particle ranges in average soft tissue with only the CEv known. This makes it possible to estimate the particle ranges in a sample of unknown material composition and density, such as a tumour, and consequently to estimate the boron concentration using equation (3). This is practically important, since a tumour commonly has a heterogeneous boron distribution, making it difficult to draw a calibration curve.

A previous attempt to modify the calibration curve using the CEv has been reported in the literature [13]. The significance of our study is that our approach makes it possible to correct for the effect of evaporation by directly using particle ranges if they are available, which may enable more accurate estimation than extrapolation from the CEv alone. Our method also makes it possible to correct for the effect of thickness differences in tissue sections. It may provide a method to compare pit density from tissue sections with different thicknesses, although using thin slices is not recommended according to Fig. 11.

In this study, we tested the validity of this concept using different thicknesses of sample-tissue sections and concentrations of boron standard solution. Although there was a gap between estimated and measured pit density, the former followed the same trend as the latter. Further study of these topics is required.

4.2 Co-localisation system for ARG

In the process of ARG, a stained image of tissue section and a pit image need to be co-localised. Several methods have been devised for this purpose. One method is to perform an etching process while protecting stained tissue sections [24]. This method enables simultaneous visualisation of both tissue sections and pits. Another method is to use reference markers for co-localisation [26]. With these markers, we can estimate the coordinates of the region of interest in the pits image from the tissue-section image using a motorised stage.

In this paper, we propose a simple co-localisation method that does not require a motorised stage (explained in sections 2.3.2 and in Fig. 2). In this method, ink-marks are put on the opposite side of the CR-39 from the tissue section using a ball-point pen; these ink-marks are protected during the chemical-etching process so that their shape does not change. Since the shape of the ink-marks is irregular, we can superimpose the two images containing the ink-marks to determine the position and rotation of corresponding features with high accuracy (Fig. 3).

4.3 Application of quantitative ARG shown in this paper and future expansion of this method

4.3.1 Proposal for quantitative ARG using the new equation and co-localisation system

In the quantitative ARG, tissue sections are put on CR-39s and irradiated with a neutron beam. After that, the CR-39s are marked for image-superimposition and attached to glass slides. Then the sections on each CR-39 are stained and photographed using a microscope. In the next step, chemical etching is performed and pictures of the pits on each CR-39 are acquired. By sealing CR-39 and glass slides using an epoxy resin-based adhesive, it is possible to maintain the location markers before and after chemical etching. Consequently, it is possible to superimpose pits in the CR-39 on the images of the tissue sections (Fig. 4), thereby enabling clarification of the quantitative spatial distribution of boron compounds in the tissue sections. The equation estimating the pit density from the boron concentration can be inverted to estimate the boron concentration from the pit density. As a result, we can acquire the boron concentration in the region of interest on the HE staining image.

We recommend calibrating the undetectability thickness each time the experiment is conducted, since there are many factors that influence its value. For the calibration, we use tissue sections with a known concentration (measured by ICP-AES or PGA) and perform the same processes as on the other sections in the experiment.

4.3.2 Possibility of future analysis using quantitative ARG

15

Knowing the micro-scale boron distribution is essential for clarifying the micro-scale dose distribution in BNCT. Absolute biological effectiveness (ABE) is one concept used to relate the micro-scale boron distribution to the dose distribution [27]. In ABE, the relationship between the distribution of boron compounds and the position of the cell nucleus is important. It is possible to make the interior and exterior of the cell nucleus the regions of interest, so that we can estimate the boron concentration in both using the quantitative ARG shown in this paper. Simulation of absorbed energy from BNCR in each region (shown in the literature [24]) is also possible. Thus, as future research, the quantitative analysis of microdistribution of boron in a case of interest is possible using the methods in this paper; this is expected to provide new insights into the microdosimetry in BNCT with the combination with ABE.

Moreover, it is practically important that, since the CR-39 is affixed to slide glass, we can stain tissue sections using the conventional staining process without requiring special techniques and laboratory instruments. In particular, the combination of this method with immunostaining methods is expected to provide new insights into the relationship between boron uptake and histological function.

4.4 Limitation

This study is not without limitations. First, the factors determining undetectability thickness are not clear experimentally. As shown in section 4.1.1, there are many potential factors that may determine the undetectability thickness, the key component of equation (3). Future work examining these factors is expected. With a better understanding of undetectability thickness, it may not be necessary to calibrate for it every time, so long as the experimental conditions are the same.

Second, in this paper, we estimated undetectability thickness experimentally under the assumption that its effects mask those of the critical angle. Then we validated this assumption by examination of the undetectability thickness using the method shown in section 2.6. According to the result in section 3.3, this assumption can be considered reasonable. However, this method may overestimate the undetectability thickness, since the globally deepest and shallowest pits may not always be in the observed area. Considering this uncertainty, examination of pit properties such as critical angle is needed in future work.

5. Conclusion

In this study, we devised an equation to estimate the pit density based on the boron concentration in ARG and on the particle ranges in the samples. The calibration-curve method is widely used in quantitative ARG; the equation shown in this paper provides a theoretical explanation for it. We validated the equation using various thicknesses of liver-tissue sections and concentrations of boron standard solution: the pit

density predicted by the equation reproduced the trend of the measured pit density. We also devised a co-localisation system between tissue-section images and pit images. Using the methods shown in this paper, boron concentration can be estimated from the pit density on the SSNTD in ARG. The Microsoft Excel file for this calculation is attached as supplementary data.

In BNCT, micro-scale boron distribution is one of the main factors to determine the treatment efficacy. The methods in this paper have the potential to reveal quantitatively the micro-scale spatial distribution of boron compounds, as described in section 4.3.2. Future research using a combination of the methods shown here with other technique such as immunostaining promises to provide new insights into BNCT. It is also expected to provide new insights into the microdosimetry in BNCT with the combination with ABE.

Appendix. The equation to estimate pit density

The probability of charged particles being detected by the SSNTD.

Through the observation of pits on the SSNTD using an optical microscope, the difference in refractive index between the surface of the SSNTD and the pits can be visualised. We assume that we cannot recognise a pit through an optical microscope if it is shallower than a certain minimum depth. Here, we define the region in which we could not recognise pits as the 'region of undetectability' (Fig. 13).

If the incident angle of the charged particle is smaller than a certain critical angle (θ_c) [28], the bulk etch rate (V_b) becomes faster than the track etch rate (V_t), with the result that no pits are formed. We define θ_{max} as

$$\theta_{max} = 90° - \theta_c. \tag{A1}$$

Fig. 14 shows a cross-sectional view centred on the point where a BNCR has occurred. In this figure, charged particles can be detected by the SSNTD within the blue fan-shaped region: the range of charged particles with the incident angle greater than the critical angle. The central angle of this region is $2\theta_{max}$.

Now, we take the coordinates of any one point on the surface of the tissue section (SSNTD side) and consider the x-axis, as shown in Fig. 15(A). Then, we consider the detection efficiency of the charged particles generated at the point of interest on the x-axis. Regarding the charged particles in the blue fan-shaped region in Fig. 14, only the particles that pass entirely through the region of undetectability in the SSNTD can be visualised and eventually detected.

Case 1: $0 < x < r\cos\theta_{max} - u$

When the blue fan-shaped region is in the position shown in Fig. 15(B), all the charged particles in this region pass through the region of undetectability. This means that all the charged particles in the blue fan-shaped region are detectable by the SSNTD, and the range of detectable angles is $2\theta_{max}$.

Because the charged particles are emitted in all directions with equal probability, we can estimate the probability ($P(x)$) of charged particles being detected by the SSNTD per solid angle, expressed as

$$P(x) = \frac{2\pi(1 - cos\theta_{max})}{4\pi} = \frac{1 - cos\theta_{max}}{2}. \tag{A2}$$

In this case, $P(x)$ is constant.

Case 2: $rcos\theta_{max} - u < x < t$

By contrast, when the blue fan-shaped region is in the position shown in Fig. 15(C), only charged particles in the red fan-shaped region (the range of charged particles with the angle of *2δ*) can pass through the region of undetectability and be detected by the SSNTD. The centre angle of the red fan-shaped region (*2δ*) is given by

$$\cos \delta = \frac{x + u}{r}. \tag{A3}$$

In this case, the probability ($P(x)$) per solid angle of charged particles being detected is as follows:

$$P(x) = \frac{2\pi(1 - cos\delta)}{4\pi} = \frac{1 - cos\delta}{2} = \frac{1}{2r}(r - u - x). \tag{A4}$$

When we consider the BNCR, we need to take into account both the alpha particles and the recoiled lithium nuclei. Hence, $P_{all}(x)$ is

$$P_{all}(x) = P_{alpha}(x) + P_{Li}(x) \tag{A5}$$

where $P_{alpha}(x)$ and $P_{Li}(x)$ are the expected detection probabilities of the alpha particles and recoiled lithium nuclei, respectively.

The estimated count of detected charged particles from BNCR.

If we define the linear density of charged particles generated on the axis of interest as ρ_l [counts/μm], the total number of particles generated in the micro-range dx [μm] at the position x [μm] is $\rho_l \cdot dx$ [counts]. As the probability of charged-particle detection at the position x [μm] is $P_{all}(x)$, the expectation value of the detected-charged-particle count is $P_{all}(x) \cdot \rho_l \, dx$ [counts]. Following equation (A5), the total number counted on the detector in the range of $0 < x < t$ (N [counts]) is

$$N = \int_0^t P_{all}(x) \cdot \rho_l \, dx = \left(\int_0^t P_{alpha}(x)dx + \int_0^t P_{Li}(x)dx \right) \cdot \rho_l \tag{A6}$$

assuming ρ_l is constant under the homogeneous boron distribution.

Here, the linear density along an axis perpendicular to a surface of area S [μm^2] is described as $\rho_l = \rho_v \cdot S$, where ρ_v is volumetric density, if the distribution of boron compounds is homogeneous. Then from the equation (A6), the estimated count of detected charged particles from the BNCR (N [counts]) in a specific area (S [μm^2]) is expressed as

$$N = \left(\int_0^t P_{alpha}(x)\, dx + \int_0^t P_{Li}(x)\, dx \right) \cdot \rho_v \cdot S. \tag{A7}$$

The volumetric density of the BNCR count (ρ_v [counts/μm^3]) is as follows:

$$\rho_v = \frac{C \cdot d \cdot N_A}{MW} \cdot \sigma \cdot \phi \cdot 10^{-18}, \tag{A8}$$

where C is the concentration of boron in the tissue [μg/g], d is the original density of the tissue [g/cm^3], MW is the molecular weight of boron [g/mol], N_A is the Avogadro constant [/mol], σ is the neutron cross-section of ^{10}B [cm^2], and ϕ is the neutron fluence [n/cm^2].

Combining equation (A7) and (A8), the estimated count of detected particles (N [counts]) is as follows:

$$N = \left(\int_0^t P_{alpha}(x)\, dx + \int_0^t P_{Li}(x)\, dx \right) \cdot \frac{N_A \cdot \sigma}{MW} \cdot 10^{-18} \cdot \phi \cdot C \cdot d \cdot S. \tag{3}$$

Here, $\int_0^t P(x)\,dx$ is described according to equations (A2, A4):

$$\int_0^t P(x)\, dx = \int_0^{r\cos\theta_{max}-u} \frac{1-\cos\theta_{max}}{2}\, dx + \int_{r\cos\theta_{max}-u}^t \frac{1}{2r}(r-u-x)\, dx. \tag{A9}$$

Therefore, we can calculate $\int_0^t P_{alpha}(x)\,dx$ and $\int_0^t P_{Li}(x)\,dx$ in equation (3) from equation (A9) by applying each parameter.

When $r\cos\theta_{max} - u < 0$, that is, the critical angle (θ_c) is smaller than $\sin^{-1}(u/r)$, the value of the critical angle does not affect the pit density because its effect is masked by the region of undetectability. In this case, equation (A9) can be rewritten as follows:

$$\int_0^t P(x)\, dx = \int_0^t \frac{1}{2r}(r-u-x)\, dx = \frac{t \cdot (2r - 2u - t)}{4r}. \tag{A10}$$

We need to accommodate the different ranges of charged particles in the water, in the dried tissue, and in the SSNTD. To do so, we convert tissue thickness (t) and undetectability thickness (u) into their equivalent values for water to be applied in equations (A9, A10). These conversions are given by

$$t_{conv} = t \cdot \frac{r_{water}}{r_{histo}},$$

$$u_{conv} = u \cdot \frac{r_{water}}{r_{SSNTD}},$$

(A11)

where r_{water}, r_{histo}, and r_{SSNTD} are the ranges in water, dried tissue, and the SSNTD, respectively.

References

[1]   Suzuki M. Boron neutron capture therapy (BNCT): a unique role in radiotherapy with a view to entering the accelerator-based BNCT era. Int J Clin Oncol 2020;25:43–50. https://doi.org/10.1007/s10147-019-01480-4.

[2]   Wittig A, Michel J, Moss RL, Stecher-Rasmussen F, Arlinghaus HF, Bendel P, et al. Boron analysis and boron imaging in biological materials for Boron Neutron Capture Therapy (BNCT). Crit Rev Oncol Hematol 2008;68:66–90. https://doi.org/10.1016/j.critrevonc.2008.03.004.

[3]   Provenzano L, Bortolussi S, González SJ, Postuma I, Protti N, Portu A, et al. Charged particle spectrometry to measure 10 B concentration in bone. Radiat Environ Biophys 2019;58:237–45. https://doi.org/10.1007/s00411-018-00776-9.

[4]   Chandra S, Lorey DR, Smith DR. Quantitative subcellular secondary ion mass spectrometry (SIMS) imaging of boron-10 and boron-11 isotopes in the same cell delivered by two combined BNCT drugs: In vitro studies on human glioblastoma T98G cells. Radiat Res 2002;157:700–10. https://doi.org/10.1667/0033-7587(2002)157[0700:QSSIMS]2.0.CO;2.

[5]   Portu A, Molinari AJ, Thorp SI, Pozzi ECC, Curotto P, Schwint AE, et al. Neutron autoradiography to study boron compound microdistribution in an oral cancer model. Int J Radiat Biol 2015;91:329–35. https://doi.org/10.3109/09553002.2014.995381.

[6]   Altieri S, Bortolussi S, Bruschi P, Chiari P, Fossati F, Stella S, et al. Neutron autoradiography imaging of selective boron uptake in human metastatic tumours. Appl Radiat Isot 2008;66:1850–5. https://doi.org/10.1016/j.apradiso.2008.05.007.

[7]   Tanaka H, Sakurai Y, Suzuki M, Masunaga SI, Takamiya K, Maruhashi A, et al. Development of a simple and rapid method of precisely identifying the position of 10B atoms in tissue: An improvement in standard alpha autoradiography. J Radiat Res 2014;55:373–80. https://doi.org/10.1093/jrr/rrt110.

[8]   Fleischer RL, Price PB, Walker RM. Nuclear tracks in solids. Berkeley: University of California Press; 1975.

[9]   Saint Martin G, Portu A, Santa Cruz GA, Bernaola OA. Stochastic simulation of track density in nuclear track detectors for 10B measurements in autoradiography. Nucl Instruments Methods Phys Res Sect B Beam Interact with Mater Atoms 2011;269:2781–5. https://doi.org/10.1016/j.nimb.2011.08.031.

[10]   Portu A, Bernaola OA, Nievas S, Liberman S, Saint Martin G. Measurement of 10B concentration through autoradiography images in polycarbonate nuclear track detectors. Radiat Meas 2011;46:1154–9. https://doi.org/10.1016/j.radmeas.2011.07.034.

[11]   Yanagie H, Ogura K, Matsumoto T, Eriguchi M, Kobayashi H. Neutron capture autoradiographic determination of 10B distributions and concentrations in biological samples for boron neutron capture therapy. Nucl Instruments Methods Phys Res Sect A Accel Spectrometers, Detect Assoc Equip 1999;424:122–8. https://doi.org/10.1016/S0168-9002(98)01284-4.

[12]   Espector NM, Portu A, Santa Cruz GA, Saint Martin G. Evaporation process in histological tissue sections for neutron autoradiography. Radiat Environ Biophys 2018;57:153–62. https://doi.org/10.1007/s00411-018-0735-8.

[13]   Espain MS, Dattoli Viegas AM, Trivillin VA, Saint Martin G, Thorp SI, Curotto P, et al. Neutron autoradiography to study the microdistribution of boron in the lung. Appl Radiat Isot 2020;165:1–9. https://doi.org/10.1016/j.apradiso.2020.109331.

[14]   Sato T, Iwamoto Y, Hashimoto S, Ogawa T, Furuta T, Abe S ichiro, et al. Features of Particle and Heavy Ion Transport code System (PHITS) version 3.02. J Nucl Sci Technol 2018;55:684–90. https://doi.org/10.1080/00223131.2017.1419890.

[15]   Pierson RN, Price DC, Wang J, Jain RK. Extracellular water measurements: organ tracer kinetics of bromide and sucrose in rats and man. Am J Physiol 1978;235. https://doi.org/10.1152/ajprenal.1978.235.3.f254.

[16]   Rana MA. CR-39 nuclear track detector: An experimental guide. Nucl Instruments Methods Phys Res Sect A Accel Spectrometers, Detect Assoc Equip 2018;910:121–6. https://doi.org/10.1016/j.nima.2018.08.077.

[17]   Watanabe T, Hattori Y, Ohta Y, Ishimura M, Nakagawa Y, Sanada Y, et al. Comparison of the pharmacokinetics between L-BPA and L-FBPA using the same administration dose and protocol: A validation study for the theranostic approach using [18F]-L-FBPA positron emission tomography in boron neutron capture therapy. BMC Cancer 2016;16:1–10. https://doi.org/10.1186/s12885-016-2913-x.

[18]   Sakurai Y, Kobayashi T. Characteristics of the KUR Heavy Water Neutron Irradiation Facility as a neutron irradiation field with variable energy spectra. Nucl Instruments Methods Phys Res Sect A Accel Spectrometers, Detect Assoc Equip 2000;453:569–96. https://doi.org/10.1016/S0168-9002(00)00465-4.

[19]   Ogawara R, Kusumoto T, Konishi T, Hamano T, Kodaira S. Detection of alpha and 7Li particles from 10B(n, α)7Li reactions using a combination of CR-39 nuclear track detector and potassium hydroxide-ethanol-water solution in accelerator-based neutron fields. Nucl Instruments Methods Phys Res Sect B Beam Interact with Mater Atoms 2020;467:9–12. https://doi.org/10.1016/j.nimb.2020.01.030.

[20]   Gadan MA, Bortolussi S, Postuma I, Ballarini F, Bruschi P, Protti N, et al. Set-up and calibration of a method to measure 10B concentration in biological samples by neutron autoradiography. Nucl Instruments Methods Phys Res Sect B Beam Interact with Mater Atoms 2012;274:51–6. https://doi.org/10.1016/j.nimb.2011.11.043.

[21]   Postuma I, Bortolussi S, Protti N, Ballarini F, Bruschi P, Ciani L, et al. An improved neutron autoradiography set-up for 10B concentration measurements in biological samples. Reports Pract Oncol Radiother 2016;21:123–8. https://doi.org/10.1016/j.rpor.2015.10.006.

[22]   Portu A, Postuma I, Gadan MA, Saint Martin G, Olivera MS, Altieri S, et al. Inter-comparison of boron concentration measurements at INFN-University of Pavia (Italy) and CNEA (Argentina). Appl Radiat Isot 2015;105:35–9. https://doi.org/10.1016/j.apradiso.2015.07.022.

[23]   Schütz CL, Brochhausen C, Hampel G, Iffland D, Kuczewski B, Otto G, et al. Intercomparison of inductively coupled plasma mass spectrometry, quantitative neutron capture radiography, and prompt gamma activation analysis for the determination of boron in biological samples. Anal Bioanal Chem 2012;404:1887–95. https://doi.org/10.1007/s00216-012-6329-4.

[24]   Solares GR, Zamenhof RG. A novel approach to the microdosimetry of neutron capture therapy. Part I. High-resolution quantitative autoradiography applied to microdosimetry in neutron capture therapy. Radiat Res 1995;144:50–8. https://doi.org/10.2307/3579235.

[25]   Kiger WS, Micca PL, Morris GM, Coderre JA. Boron microquantification in oral muscosa and skin following administration of a neutron capture therapy agent. Radiat Prot Dosimetry 2002;99:409–12. https://doi.org/10.1093/oxfordjournals.rpd.a006820.

[26] Postuma I, Sommi P, Vitali A, Shu D, Martino G di, Cansolino L, et al. Colocalization of tracks from boron neutron capture reactions and images of isolated cells. Appl Radiat Isot 2021;167:109353. https://doi.org/10.1016/j.apradiso.2020.109353.

[27] Ono K, Tanaka H, Tamari Y, Watanabe T, Suzuki M, Masunaga SI. Proposal for determining absolute biological effectiveness of boron neutron capture therapy - The effect of 10 B(n,α) 7 Li dose can be predicted from the nucleocytoplasmic ratio or the cell size. J Radiat Res 2019;60:29–36. https://doi.org/10.1093/jrr/rry080.

[28] Somogyi G. Development of etched nuclear tracks. Nucl Instruments Methods 1980;173:21–42. https://doi.org/10.1016/0029-554X(80)90565-0.
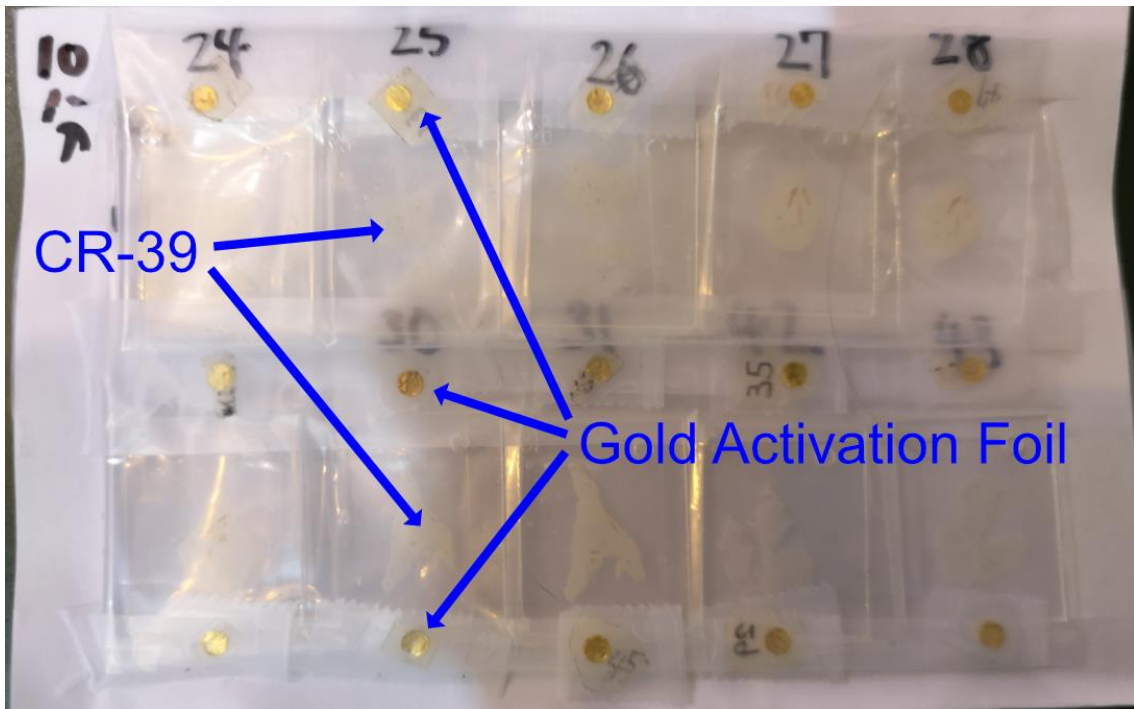
Fig. 1

Irradiation of liver sections. The liver sections are put on the CR-39 solid-state nuclear track detectors and irradiated. Neutron fluence was measured using gold activation foils placed above and below each CR-39.
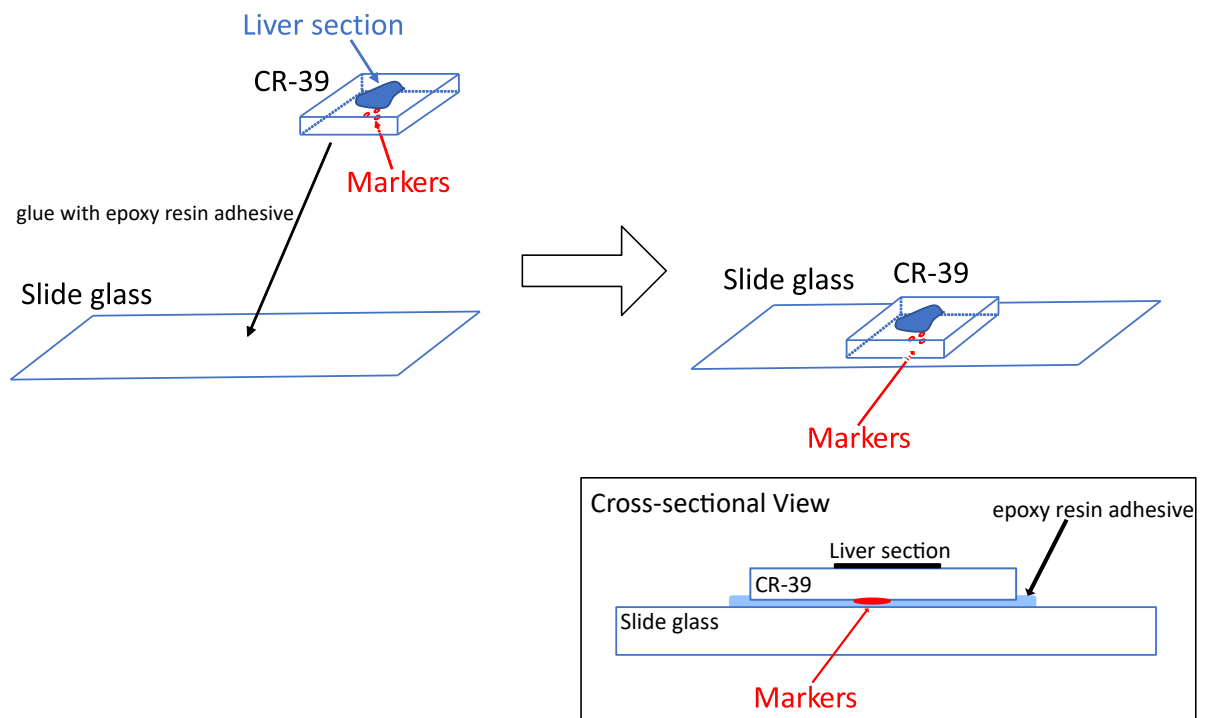
Fig. 2

Co-localisation technique for autoradiography. Using a ball-point pen, we put small ink-marks on the opposite side of the CR-39 solid-state nuclear track detector from the liver section, for use later in the superposition of the histological and pit images. Then the CR-39 was placed on the slide glass using epoxy resin adhesive. The ink-marks, sealed in epoxy between the CR-39 and slide glass, were thus protected during the chemical-etching process.
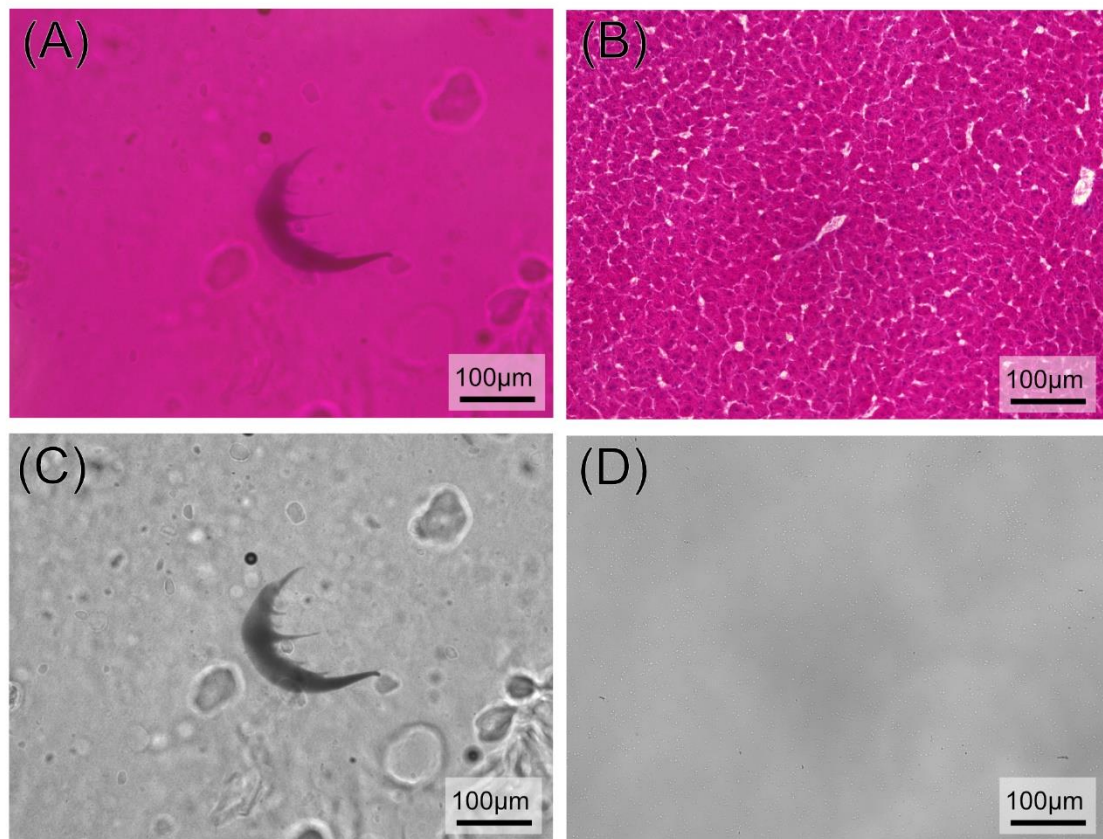
Fig. 3

(A) and (B) are the ink-mark image and corresponding Hematoxylin–Eosin-staining image, respectively. These images represent the same coordinates but are focused in different planes (as explained in section 2.3.2). (C) and (D) are the corresponding post-etching ink-mark image and pit image, respectively. These images are also at the same coordinates and focused in different planes (as explained in section 2.3.2). Since the shape of the ink-mark made by the ball-point pen is irregular, it is not difficult to match its position and rotation in images (A) and (C). Then images (B) and (D) can be superimposed by the same transformation of position and angle. Note that, in image (D), the pits can be hardly identified because of the magnitude of the image.
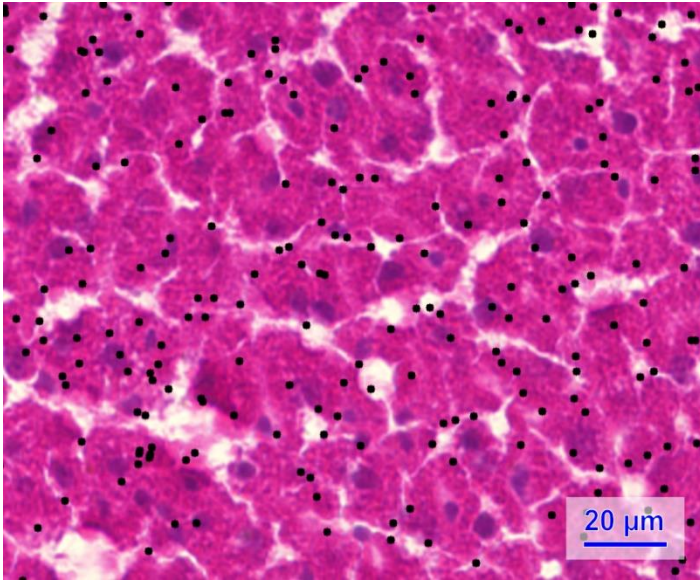
Fig. 4

Superposition of image showing pits on CR-39 on an Hematoxylin–Eosin-staining image of a liver section. The small black dots represent the pits on the CR-39, i.e. the boron–neutron-capture reaction locations.
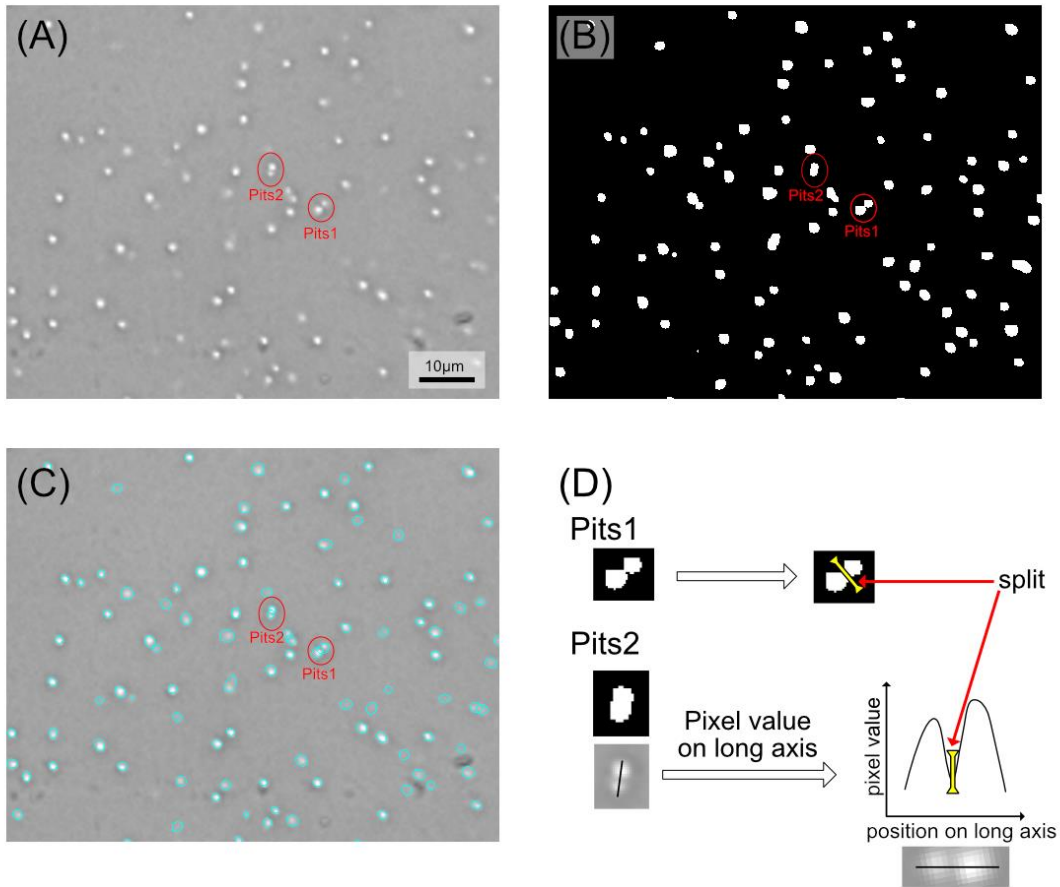
Fig. 5

In the pit-detection algorithm, overlapping pits need to be separated. (A) is the original image of the pits. Using the binarised image (B), the pits are identified automatically. However, Pits1 and Pits2 in image (C) are identified as one pit, whereas they are two overlapping pits. (D) shows the separating process. Pits1 can be separated by the detection of convexity defects. On the other hand, Pits2 does not have convexity defects. In such cases, we acquire the pixel values on the long axis of Pits2 as a graph, which has two peaks and one nadir. Then we can separate it into two pits at the nadir point in the graph.
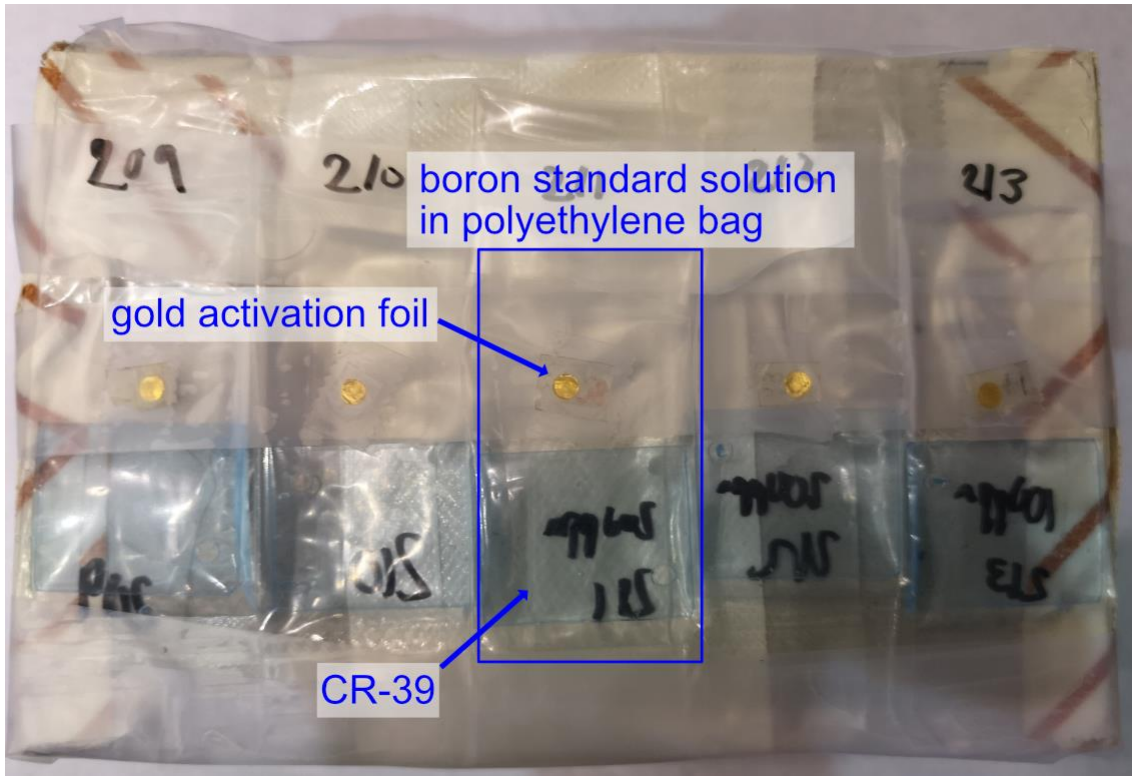
Fig. 6

Irradiation of boron standard solution. Boron standard solution and CR-39 are packed in a low-density polyethylene bag. Gold activation foil is attached to the surface of the bag to measure irradiated fluence.
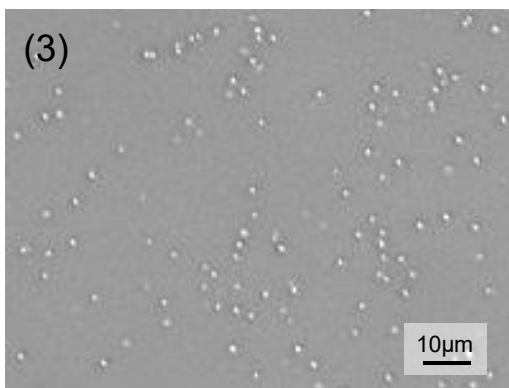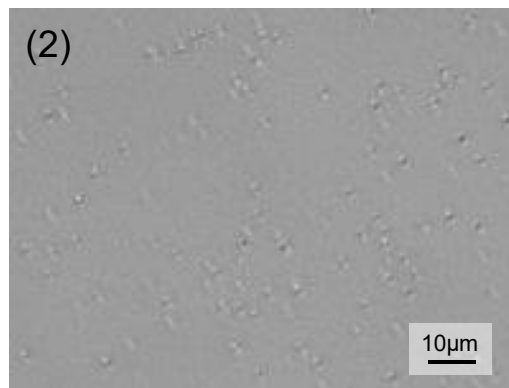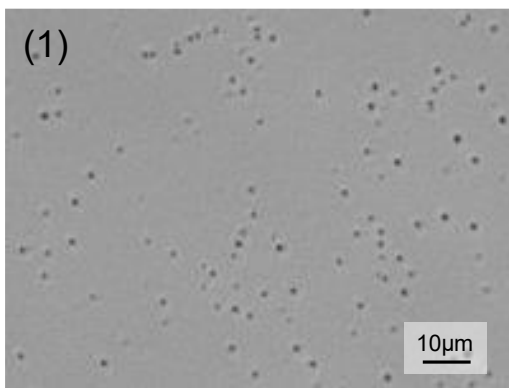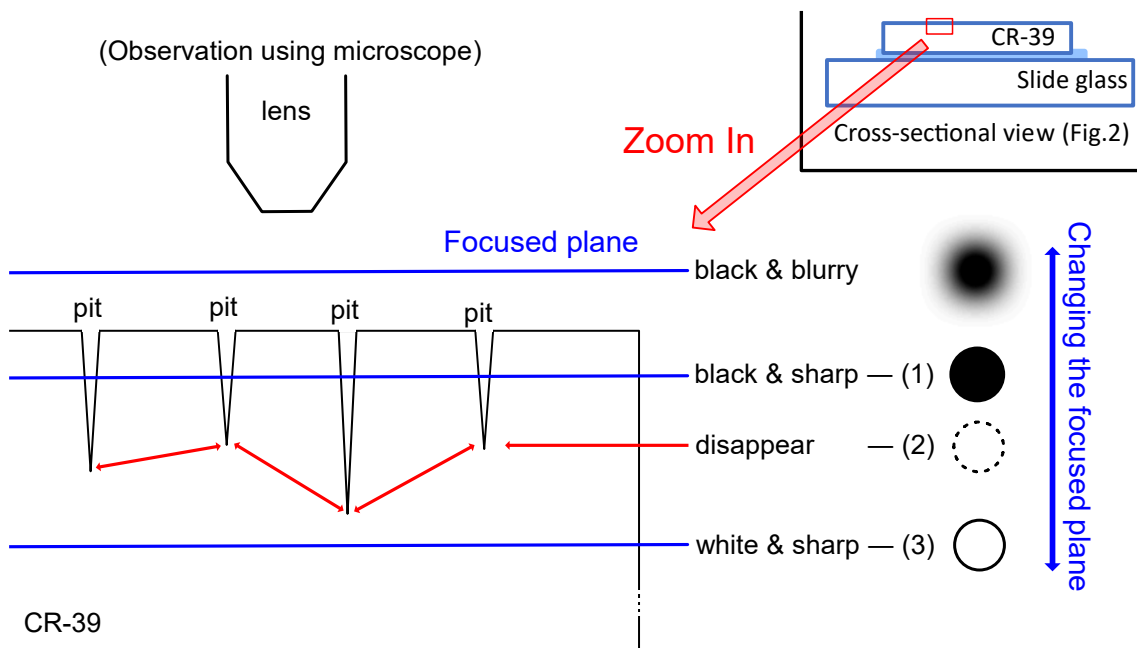
Fig. 7

Relationship between the focal plane and the pit image in optical-microscope observations. Focused

planes are shown as blue lines. If the focused plane is in front of the surface of the CR-39, the pits are

observed as black and blurry pits. When the focused plane is deeper, the shape of the pit changes from (1) to (3). If the focused plane is at the bottom of the pit, the pit disappears, as shown in (2).
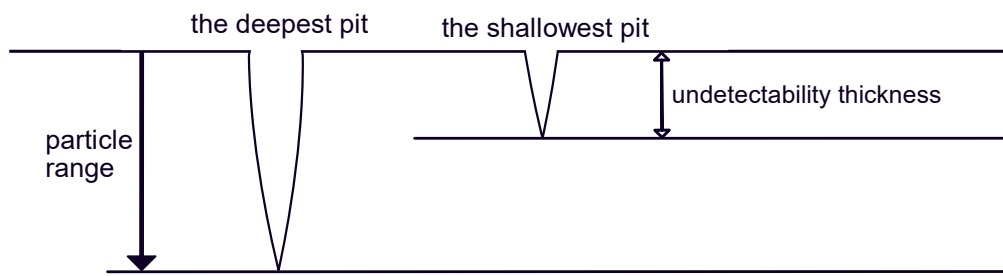
Fig. 8

Schematic drawing of undetectability-thickness estimation. The depth of the deepest pit is equal to the particle range and the depth of the shallowest pit is equal to the undetectability thickness. Since we can acquire only the relative distribution of the pit depths, we cannot estimate the undetectability thickness directly. Instead, we can find the difference between the depths of the deepest and shallowest pits and estimate the undetectability thickness by subtracting this value from the particle range.
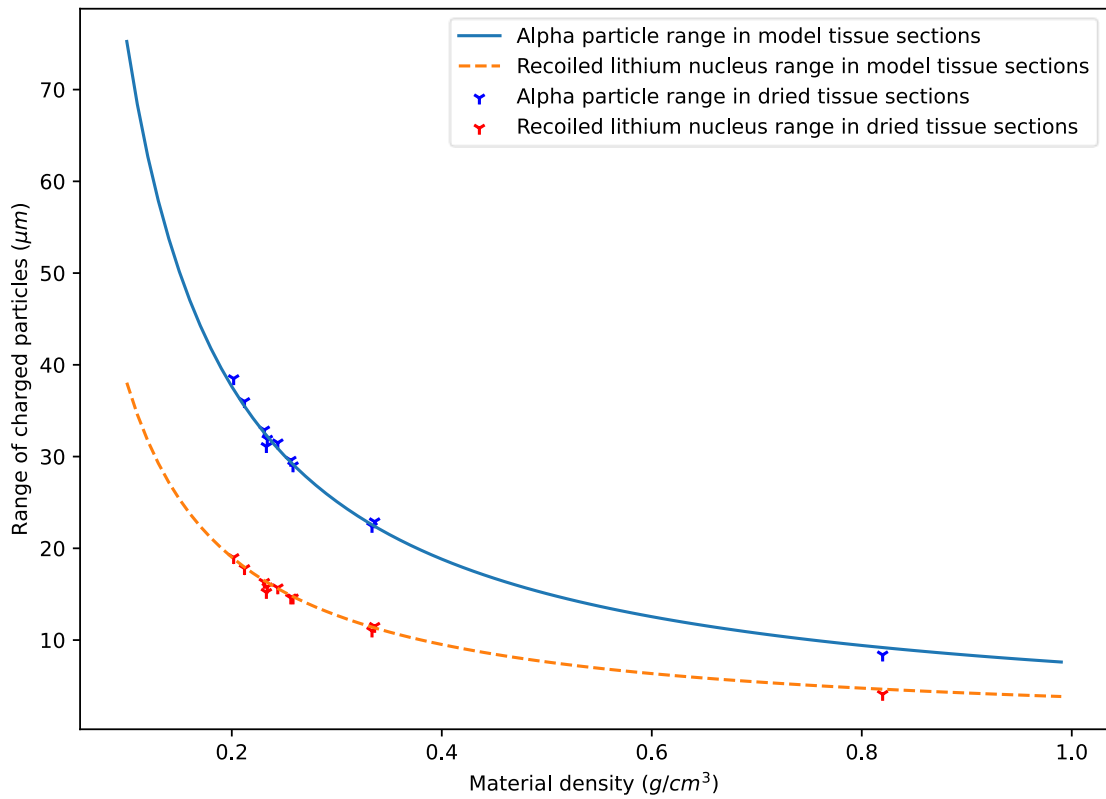
Fig. 9

Relationship between material density and ranges of the charged particles. The blue solid and orange dashed lines represent the estimated ranges based on the elemental composition of average soft tissue. The blue and red 'Y' shapes represent experimental data collected in this study or reported in the literature (based on Table 2(A)).
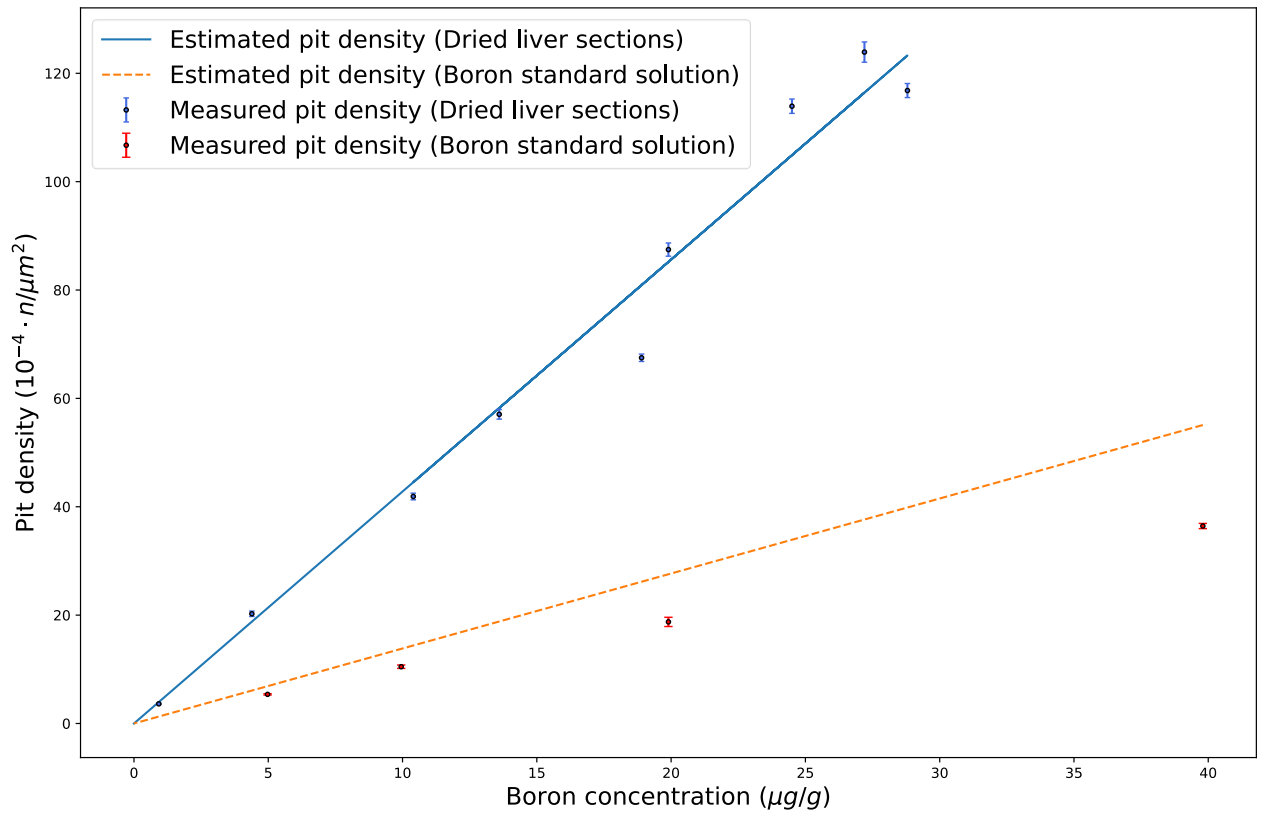
Fig. 10

The boron concentration in dried liver sections and the pit density on CR-39 are shown as blue dots and a blue solid line. The error bars associated with the measured pit density in this case show standard error (n = 10). The boron concentration in the boron standard solution and the pit density on CR-39 are shown as orange dots and an orange dashed line. The error bars associated with the measured pit density in this case show standard error (n = 8). The pit density is shown as the counts per $100 \times 100\mu m$ square.
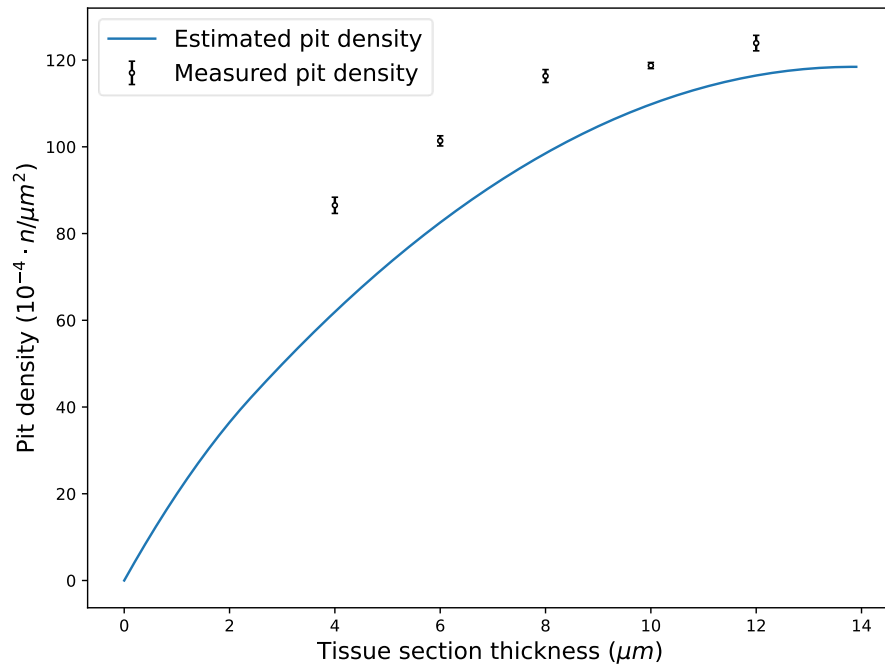
Fig. 11

Relationship between the thickness of dried liver sections and the pit density on CR-39. The error bars associated with the measured pit density show standard error (n = 10). The pit density is shown as the counts per $100 \times 100\mu m$ square.
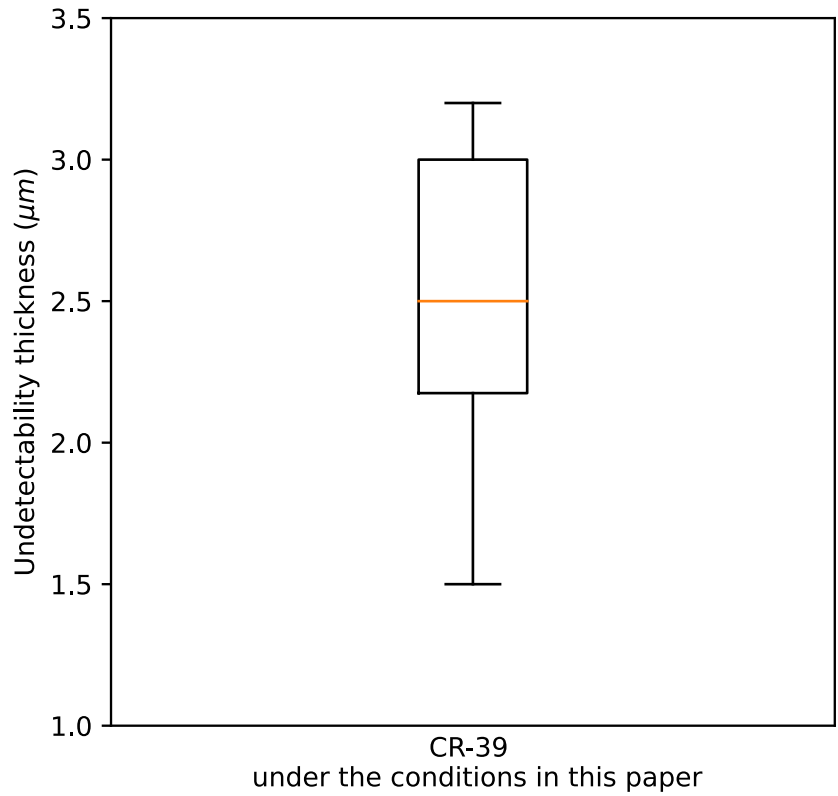
Fig. 12

Distribution of the measured undetectability thickness of CR-39 under the experimental conditions shown in this paper. This distribution was estimated by subtracting the difference between the depths of the deepest and shallowest pits from the particle range (as shown in Fig. 8). The box indicates the interquartile range. The interval of the population mean of the undetectability thickness is 2.30 < undetectability thickness < 2.71 (95% confidence interval).
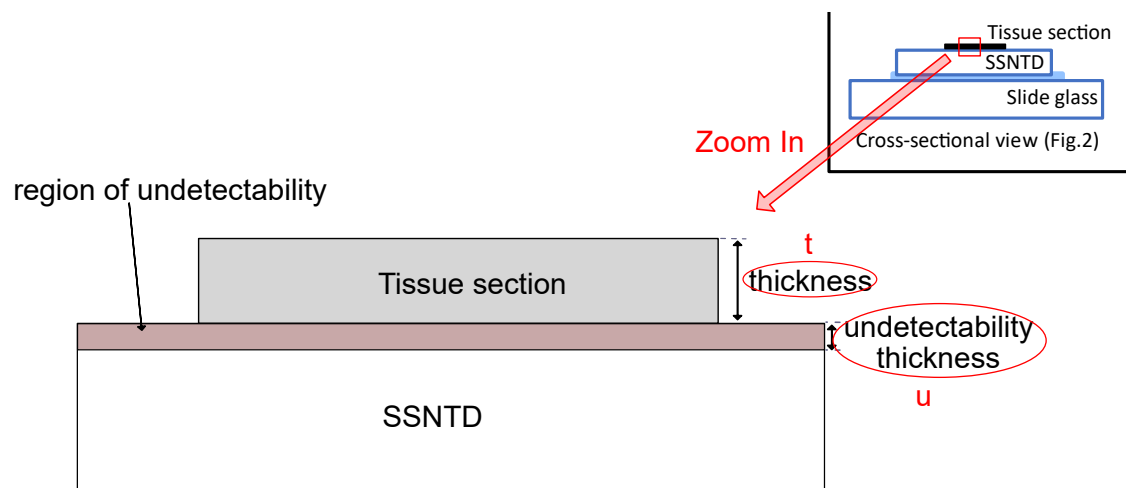
Fig. 13

Schematic drawing of a tissue section on a solid-state nuclear track detector (SSNTD) in autoradiography (see Fig. 2). A magnified view of the tissue section and surface of the SSNTD is shown here. In the SSNTD, it is assumed that there is a certain region defined as the region of undetectability in which pits cannot be detected. (u: undetectability thickness, t: tissue-section thickness)
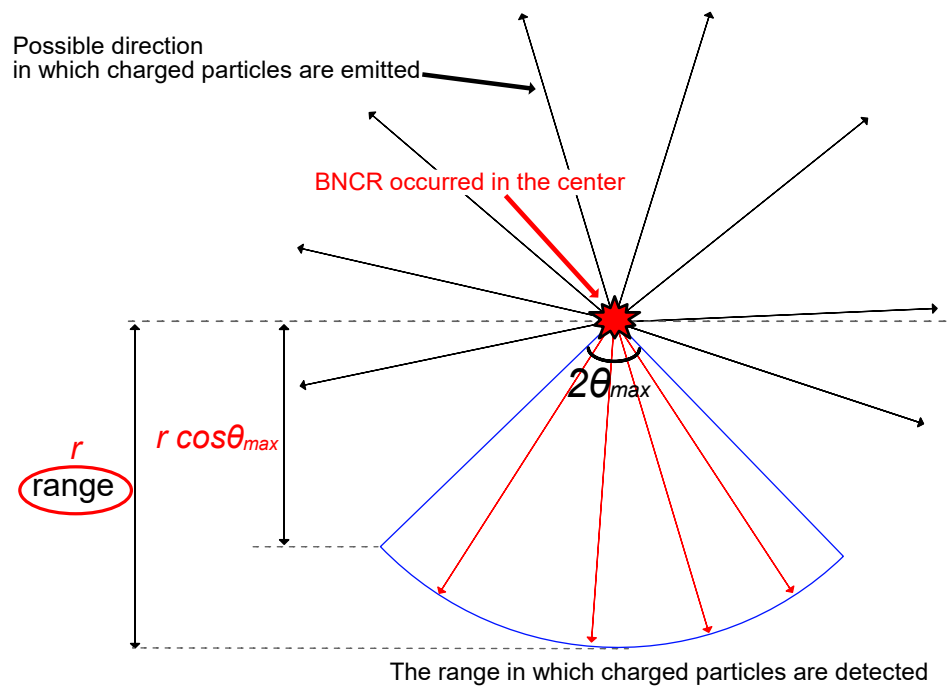
Fig. 14

Cross-sectional view centred on the point where a boron neutron-capture reaction has occurred. Charged particles are emitted in all directions equally. The angle $\theta_{max} = 90° - \theta_c$ where θ_c is the critical angle. The range in which the charged particles are detected on the solid-state nuclear track detector is restricted to the blue bounded region. (r: the range of charged particle)
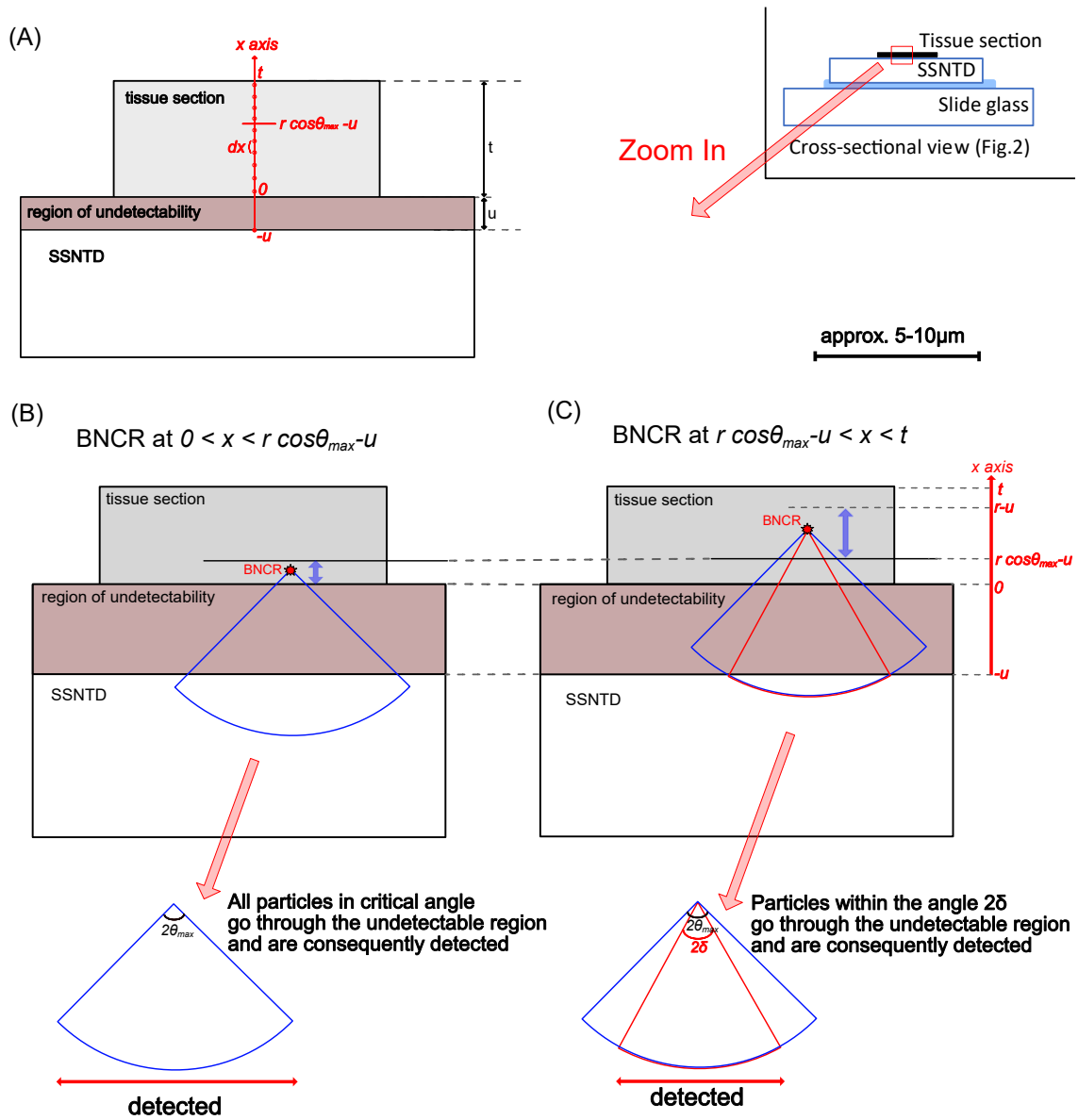
Fig. 15

Schematic drawing of boron neutron-capture reaction (BNCR) and charged-particle detection. (A) We take the origin on the surface of the solid-state nuclear track detector (SSNTD) and the x-axis perpendicular to the tissue section. Here, u is the thickness of the region of undetectability, t is the thickness of the tissue section, and r is the range of the charged particle. (B, C) Assuming that BNCRs occur along the axis, we consider the probability that pits arising from them are detected by SSNTD. The blue fan-shape is the range in which charged particles are detected considering the critical angle shown in Fig. 14. There are two cases: (B) all the particles in the blue fan-shaped region are detected, (C) only the particles in the red fan-shaped region (angle 2δ) are detected.

Table 1

Relationship of administered L-BPA dosage, sacrifice timing and tissue section thickness. Mice nos. 1–6 and nos. 7-9 were experimented on separately. The boron concentration measured by ICP-AES is also shown.

Mouse No.	L-BPA dosage	Sacrifice timing	Tissue sections thickness	Boron concentration
1	500 mg/kg	1h	10 μm	10.4 μg/g
2	1000 mg/kg	1h	10 μm	18.9 μg/g
3	1500 mg/kg	1h	10 μm	19.9 μg/g
4	2000 mg/kg	1h	10 μm	28.8 μg/g
5	500 mg/kg	3h	10 μm	4.39 μg/g
6	500 mg/kg	17h	10 μm	0.924 μg/g
7	500 mg/kg	1h	12 μm	13.6 μg/g
8	1000 mg/kg	1h	12 μm	24.5 μg/g
9	2000 mg/kg (separately)	1h+1h *	4-12 μm	27.2 μg/g

* L-BPA was administered every hour in two doses of 1000 mg/kg. One hour after the last administration, the mice were sacrificed.

Table 2

(A) Percentages of dried weight and mean ranges of the charged particles in various organs.

Organs	Material density (ICRU46)	Evaporation Coefficient (CEv)		Mean ranges of charged particles	
		Experimental data	Reported data (Rat)	Alpha particles	Recoiled lithium nuclei
Liver	1.06 g/cm^3	0.317	0.292	22.9 μm	11.5 μm
Kidney	1.05 g/cm^3	0.244	0.235	29.6 μm	14.6 μm
Muscle	1.05 g/cm^3	0.246	0.257	29.0 μm	14.6 μm
Spleen	1.06 g/cm^3	0.230	0.199	31.5 μm	15.7 μm
Tumour (CT26)		0.196	-	-	-
Skin	1.09 g/cm^3	–	0.306	22.4 μm	11.0 μm
Adipose	0.95 g/cm^3	–	0.863	8.38 μm	4.09 μm
Small intestine	1.03 g/cm^3	–	0.227	31.9 μm	15.8 μm
Lung	1.04 g/cm^3	–	0.194	38.5 μm	19.0 μm
Brain	1.04 g/cm^3	–	0.224	31.1 μm	15.2 μm
Heart	1.05 g/cm^3	–	0.202	36.0 μm	17.8 μm
Thyroid	1.05 g/cm^3	–	0.220	32.9 μm	16.3 μm

（B）The estimated mean ranges of charged particles in water and CR-39.

Materials	Mean ranges of charged particles	
	Alpha particles	Recoiled lithium nuclei
Water	7.72 μm	3.98 μm
CR-39	6.00 μm	3.00 μm